Effect of Cr Addition on Cu-Mn Spinel/delafossite Redox Couples for Medium-high Temperature Thermochemical Energy Storage

Xiaoyu Chen[a], Mitsuhiro Kubota[a*], Noriyuki Kobayashi[a], Seiji Yamashita[b], Hideki Kita[a]

[a]Nagoya University, Graduate school of Engineering, Department of Chemical Systems Engineering, Nagoya 4648603, Japan

[b]Nagoya University, Graduate school of Engineering, Department of Materials Process Engineering, Nagoya 4648603, Japan

Abstract: In this study, we developed $Cu(Cr_xMn_{1-x})_2O_4/CuCr_xMn_{1-x}O_2$ (x = 0, 0.1, 0.3, 0.5, 0.7, 0.9, 1.0) redox couples for medium-high temperature (500 – 1000 °C) redox-type thermochemical energy storage system. Structural characterization, redox behavior, re-oxidation behavior and kinetic analysis, heat storage capacity, and cyclability were investigated using SEM-EDS, XRD, TGA, and DSC, respectively. When x = 0 – 0.5, samples exhibited decreasing operating temperature with increasing amount of Cr, whereas they lost their reversibility when x > 0.5. R-$CuCr_{0.1}Mn_{0.9}$ and R-$CuCr_{0.3}Mn_{0.7}$ showed a faster reaction rate than R-CuMn because samples with small amount of Cr required lower activation energy (E_a) for re-oxidation. The DSC results showed that a small amount of Cr improved the heat storage capacity of material. In the cyclability test, the introduction of a small amount of Cr did not cause the deterioration of cyclic properties.

Keywords: *heat storage, redox-type TCES, medium-high temperature, Cr-doping, copper-manganese oxide*

1. Introduction

Thermal energy storage systems can be classified into conventional sensible, latent, and thermochemical energy storage (TCES) systems[1]. TCES systems have attracted considerable attention in the field of thermal energy storage and utilization because of its large energy-storage density, wide operating temperature range, and theoretically unlimited transportation distance[2]. Generally, TCES systems are based on reversible chemical reactions in which thermal energy is stored in the form of chemical bonds.

$$A_{solid} + heat \rightarrow B_{solid} + C_{gas} \uparrow \qquad (1)$$

At present, TCES systems are subdivided into specific research fields on the basis of reaction media, such as redox (O_2), carbonate (CO_2), hydroxide (H_2O), ammonia (NH_3), metal sulfate (SO_2), and metal hydride (H_2) systems[3,4]. Among these TCES systems, redox-type TCES systems have received widespread attention because they do not require any tank for gaseous products. Theoretically, oxygen can be easily extracted from the atmosphere, and it can also function as a heat-transfer fluid.

The development of renewable energy (such as solar, wind, and biomass energy) technology has

*Corresponding author. Email-address: kubota.mitsuhiro@material.nagoya-u.ac.jp

become particularly important owing to the considerable attention received by the concept of "Carbon Neutrality". Recently, redox-type TCES systems have been investigated to match the electrical demand and overcome instability of concentrated solar power (CSP) plants[3,5,6,7,8], because solar energy is extremely vulnerable to weather conditions. Owing to the inherently high reduction/oxidation temperatures of metal oxides and considerations of energy conversion efficiency, redox-type TCES systems are often designed for high temperature ranges (>1000 °C) thermal energy storage in CSP. Currently, research on the application of CSP has progressed beyond the development of TCES materials and evolved to the mg-level-scale[9], fluidized-bed-scale[10], and 5kW-scale[11].

Nevertheless, other thermal energy storage fields, such as exhaust gas heat recycling of steel and non-ferrous metals industry, transportation equipment industry, and in-car heating system of electric vehicles during the winter, can be also benefited from advanced redox-type TCES systems owing to the economic and volume advantages of compact heat storage equipment; in particular, the design of electric vehicles includes volume restrictions. From a practical perspective, such applications are unsuitable in high temperature range, or high temperature environments are not required.

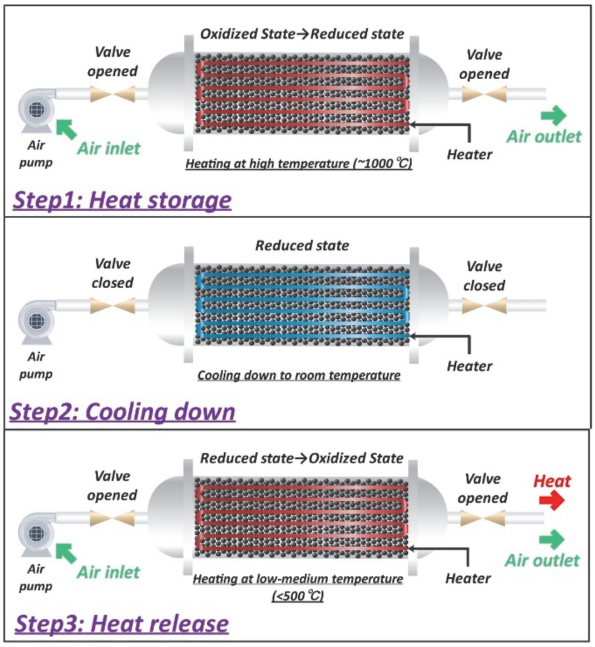

Figure 1 Schematic of the operation of medium-high temperature redox-type TCES

Figure 1 shows the schematic of the medium-high temperature redox-type TCES system. First, the material is heated from its oxidized state to reduced state by external heat sources (electric heater, etc.), and the valves of the gas inlet and outlet are opened to sweep the oxygen generated by the reduction reaction. In the second step, the two valves are first closed, and the material is cooled to room temperature at a lower pO_2 (to prevent re-oxidation). Hence, this step yields the reduced-state material, and the thermal energy is stored in the form of chemical substances. In the last step, the valves are reopened, and the material is heated to medium temperature (<500 °C) by the electric heater. Once re-oxidation reaction occurs, the stored heat is released and the temperature is maintained by the reaction itself; therefore, additional heat sources are no longer required.

The inherent limitations of redox-type TCES materials have hindered the development of medium-high temperature (500 – 1000 °C) technology. This has resulted in wastage of energy and deficiency in redox-type TCES. On the other hand, thermal energy is usually considered as a low-grade form of energy. In particular, according to the exergy theory and limitation of the Carnot cycle, it is more difficult to recycle when the temperature of heat source decreases. In our previous study, we investigated the feasibility of Sr-based perovskites for medium-high-temperature redox-type TCES purposes[12]. However, the redox reaction of Sr-based perovskites is not accompanied by an obvious phase change, which results in limited heat storage capacity (<100 kJ/kg) although their re-oxidation reaction occurred at relatively lower temperatures. In early years, Kato et al. investigated the oxygen storage capacity of delafossite $CuMO_2$ (M = Al, Fe, Mn, Ge, La, and Y)[13,14] and claimed that their oxygen storage behavior, namely re-oxidation reaction, can occur at low temperatures (300 – 600 °C). Later, our research group[15] and Fan et al.[16] studied the feasibility of using $CuMn_2O_4$/$CuMnO_2$ redox couple for TCES purposes. We observed that the MO_x polyhedral structure existing in the spinel/delafossite redox couple may play an important role, allowing the reduced-state material to re-oxidize at the temperatures much lower than their onset oxidation temperatures. Recently, Portilla-Nieto et al.[17] (CIC energiGUNE) reported the effects of Ni-doping on Co_3O_4, which is a well-known material in TCES field. They reported that $Co_{2.4}Ni_{2.6}O_4$ exhibited the lowest reduction temperature (735 – 800 °C) in the $Co_{3-x}Ni_xO_4$ system ($0 \leq x \leq 1$) and maintained relatively good reactivity, which suggested that it is feasible to minimize the reduction/oxidation temperature of TCES material via element doping.

However, Ni appears to be unsuitable as a good dopant the Cu-Mn oxide system in this work. According to the phase diagram of Cu-Ni-O[18], Ni may form a hard-to-decompose solid solution $(Ni,Cu)O_{ss}$ with the Cu element in $CuMn_2O_4$/$CuMnO_2$ redox couple, which increase the operating temperature. Very recently, Carrillo et al.[19] investigated the doping effect of Cr in the Mn_2O_3/Mn_3O_4 redox couple for TCES applications, and observed that Mn_2O_3/Mn_3O_4 with 5% Cr doping exhibited better cyclability, faster re-oxidation rate, and smaller thermal hysteresis. As mentioned above, the effects of Mn and Fe on copper oxides have been investigated in our previous study[15]. As a transition metal, the properties of Cr closely resemble those of Mn and Fe. The Cu-Cr-O phase diagram (Fig.S1) indicates that $CuCr_2O_4$ can decompose into $CuCrO_2$ at 782 °C, which is much lower than corresponding temperatures for $CuMn_2O_4$ (969 °C) and $CuFe_2O_4$ (1030 °C). This implies that the reduction temperature of the material may decrease when the atomic number of B site in the spinel decreases. However, our preliminary experiments indicated that the reaction between $CuCr_2O_4$ and

$CuCrO_2$ lacks reversibility.

In this study, Cr works as an addition on Cu-Mn spinel/delafossite redox couple in the exploration of novel medium-high temperature (500 – 1000 °C) TCES materials. Structural characterization was performed using X-ray diffraction (XRD). Redox, re-oxidation, cyclability behaviors were studied using thermogravimetric analysis (TGA) in the temperature range of 500 – 1000 °C. The kinetics of re-oxidation were analyzed using data extracted from TGA. Oxidation enthalpy of each reduced-state sample was measured by differential scanning calorimetry (DSC) with an isothermal oxidation method.

2. Experimental approach

2.1 Synthesis

$Cu(Cr_xMn_{1-x})_2O_4$ (oxidized state, denoted as O-$CuCr_xMn_{1-x}$) and $CuCr_xMn_{1-x}O_2$ (reduced state, denoted as R-$CuCr_xMn_{1-x}$) were synthesized using a modified Pechini method[20]. Mixtures of $Cu(NO_3)_2·3H_2O$, $Cr(NO_3)_2·9H_2O$, and $Mn(NO_3)_2·6H_2O$ in the molar ratio 1 : x : (1-x) were dissolved in deionized water (x = 0, 0.1, 0.3, 0.5, 0.7, 0.9, 1.0). Citric acid and ethylene glycol were added to the solution as reactants for the polyesterification reaction. The solution was evaporated at 120 °C for 4 h and dried in a vacuum oven for 24 h. After pre-calcining process at 500 °C for 1 h, the obtained powder was heated at 1000 °C for 12 h (air atmosphere for O-$CuCr_xMn_{1-x}$, Ar atmosphere for R-$CuCr_xMn_{1-x}$).

2.2 Material characterization

The tolerance factor (τ) of spinel (AB_2O_4) can be calculated using the following equation:

$$\tau = \frac{\sqrt{3}(R_B + R_O)}{2(R_A + R_O)} \tag{2}$$

where τ, R_A, R_B, and R_O are the tolerance factor, the ionic radii at A site, the ionic radii at B site, and R_O is the ionic radii of oxygen, respectively. The Shannon effective ionic radii (IR), in accordance with the coordination number (CN), was used to calculate τ, for example, CN = 4 for $A_{tetrahedra}$, CN = 6 for $B_{octahedra}$, and CN = 4 for O. In addition, since there are two elements (Cr and Mn) on B site, the corresponding coefficients must be multiplied with each element's radii during the calculation.

To verify the elemental ratios of Cu, Cr, and Mn in the system, the as-prepared samples were observed using scanning electron microscopy (SEM) (JSM-7500F, JEOL) equipped with energy dispersive spectroscopy (EDS) (ESCALAB250Xi, Thermo Fisher Scientific). O-$CuCr_xMn_{1-x}$ was chosen as a representative for analysis because O-$CuCr_xMn_{1-x}$ and R-$CuCr_xMn_{1-x}$ were derived from the same precursor.

The structure and phase composition of the as-prepared O-$CuCr_xMn_{1-x}$ and R-$CuCr_xMn_{1-x}$ samples were investigated using XRD (SmartLab, Rigaku Corp.) in the 2θ range of 15 – 90°. The phase composition of each sample was analyzed using PDXL2 (Rigaku Data Analysis Software).

2.3 Redox behavior

The redox behavior of the O-$CuCr_xMn_{1-x}$ sample was investigated using TGA (STA7300, HITACHI High-Tech Science Corp.). The TGA temperature program consisted of heating/cooling steps from room temperature to 1000 °C at a rate of 20 °C/min under synthetic air flow (200 ml/min).

2.4 Re-oxidation behavior and kinetic analysis

The R-$CuCr_xMn_{1-x}$ sample was heated from room temperature to 1000 °C at a rate of 20 °C/min under synthetic air flow (200 ml/min). The heating process of each R-$CuCr_xMn_{1-x}$ sample was extracted for investigating of re-oxidation behavior.

In re-oxidation kinetic analysis, the kinetic triplet parameters (A, E_a, $f(\alpha)$) of R-$CuCr_xMn_{1-x}$ ($x = 0$, 0.1, 0.3) were analyzed using non-isothermal heating experiments at different heating ramps ($\beta = 5$, 10, 15, and 20 °C/min, $\beta = dT/dt$) under synthetic air atmosphere (200 mL/min). To avoid mass transfer limitations, ca. 15 mg of material was placed in a Pt crucible (95 μL).

In the non-isothermal method, the activation energy E_a can be computed directly without the previous knowledge of the reaction model $f(\alpha)$. After obtaining E_a, the reaction model $f(\alpha)$ can be determined using the $g(\alpha)/g(0.5)$ master plots of different existing reaction models. Some common reaction models for solid-state kinetics are listed in Table S1. Finally, the pre-exponential factor A can be easily generated by an internal relationship with the other two parameters.

2.5 Oxidation enthalpy measurement

The R-$CuCr_xMn_{1-x}$ sample was chosen for oxidation enthalpy measurements performed using DSC (DSC-60, Shimadzu Corp.) via the isothermal oxidation method. R-$CuCr_xMn_{1-x}$ was heated to an appropriate temperature under N_2 protection, and the gas atmosphere was shifted to synthetic air when temperature stabilized. The introduction of oxygen caused an oxidation reaction that released heat rapidly. The exothermic peak was simultaneously monitored by DSC. Additional experiment details can be found in our previous work[15].

2.6 Cyclability test

O-$CuCr_xMn_{1-x}$ ($x = 0$, 0.1, 0.3) was chosen for 20 cycles heating/cooling cyclability tests in the range of 500 – 1000 °C. The XRD patterns before and after cycling were compared to verify the compositional stability of the materials.

3. Results and discussion

3.1 Material Characterization

The tolerance factor (τ) and elemental ratios of O-$CuCr_xMn_{1-x}$ are summarized in Table 1. The tolerance factor is a very useful tool to evaluate the phase stability of a certain crystal structure (e.g., perovskite[21,22], spinel[23]) from initial state. In O-$CuCr_xMn_{1-x}$ systems, τ increases with the amount of Cr added; however, a large τ makes the spinel phase unstable and susceptible to decompose.

The atomic number of Cu was set to one as a reference. The results showed that the ratios of Cr and Mn elements were very close to those of the raw materials that introduced during synthesis. Therefore, we can conclude that using the Pechini method, the components of materials are consistent with our expected results.

Table 1 Tolerance factor and elemental ratios of O-$CuCr_xMn_{1-x}$

Sample	**Tolerance factor τ**	**Cu**	**Cr**	**Mn**
O-CuMn	0.910	1.00±0.00	0.00±0.00	0.96±0.04
O-$CuCr_{0.1}Mn_{0.9}$	0.913	1.00±0.00	0.10±0.00	0.83±0.01
O-$CuCr_{0.3}Mn_{0.7}$	0.918	1.00±0.00	0.30±0.00	0.67±0.01
O-$CuCr_{0.5}Mn_{0.5}$	0.924	1.00±0.00	0.49±0.01	0.47±0.01
O-$CuCr_{0.7}Mn_{0.3}$	0.929	1.00±0.00	0.70±0.02	0.29±0.04
O-$CuCr_{0.9}Mn_{0.1}$	0.934	1.00±0.00	0.96±0.02	0.11±0.01
O-CuCr	0.937	1.00±0.00	1.07±0.02	0.00±0.00

The XRD patterns of O-$CuCr_xMn_{1-x}$ and R-$CuCr_xMn_{1-x}$ ($x = 0, 0.1, 0.3, 0.5, 0.7, 0.9, 1.0$) are shown in Figure 2. Interestingly, there are no obvious differences in the XRD patterns of O-$CuCr_xMn_{1-x}$ when $x \leq 0.5$. A comparison with standard ICDD PDF card of $CuMn_2O_4$ (01-074-1919) and $CuCr_2O_4$ (01-077-4323) indicates that the crystal systems of both materials are cubic. Furthermore, the two phases possess very similar lattice constant and peak positions, and the Cr peak cannot be distinguished from XRD pattern of O-$CuCr_xMn_{1-x}$ ($x \leq 0.5$). In addition, a small amount of CuO is also present in all the oxidized state sample (Figure 2a, 2θ = 32.4°, 35.2°, 38.8°, 48.8°, 72.4°) but not in reduced sample, which is consistent with our previous report[15].

Although O-$CuCr_{0.9}Mn_{0.1}$ and O-CuCr were prepared in air ($pO_2 = 0.21$), which was regarded as an oxidizing atmosphere, they still exhibited the same XRD pattern as R-$CuCr_{0.9}Mn_{0.1}$ and R-CuCr. When the precursor was heated, it was initially converted to spinel-type $Cu(Cr_xMn_{1-x})_2O_4$ and reduced to delafossite with increasing temperatures. However, the Cr-rich sample ($x \geq 0.9$) may lack the ability to re-oxidize into spinel when cooled in air, which may be related to large τ values. Moreover, the $CuCrO_2$ characteristic peaks were also observed in the XRD pattern of O-$CuCr_{0.7}Mn_{0.3}$ (2θ = 31.3°, 36.3°, 40.8°, 55.7°, 61.6°, and 62.3°). Therefore, when $x \geq 0.7$, the O-$CuCr_xMn_{1-x}$ system exhibits a spinel + delafossite mixed phase instead of an ideal solid solution.

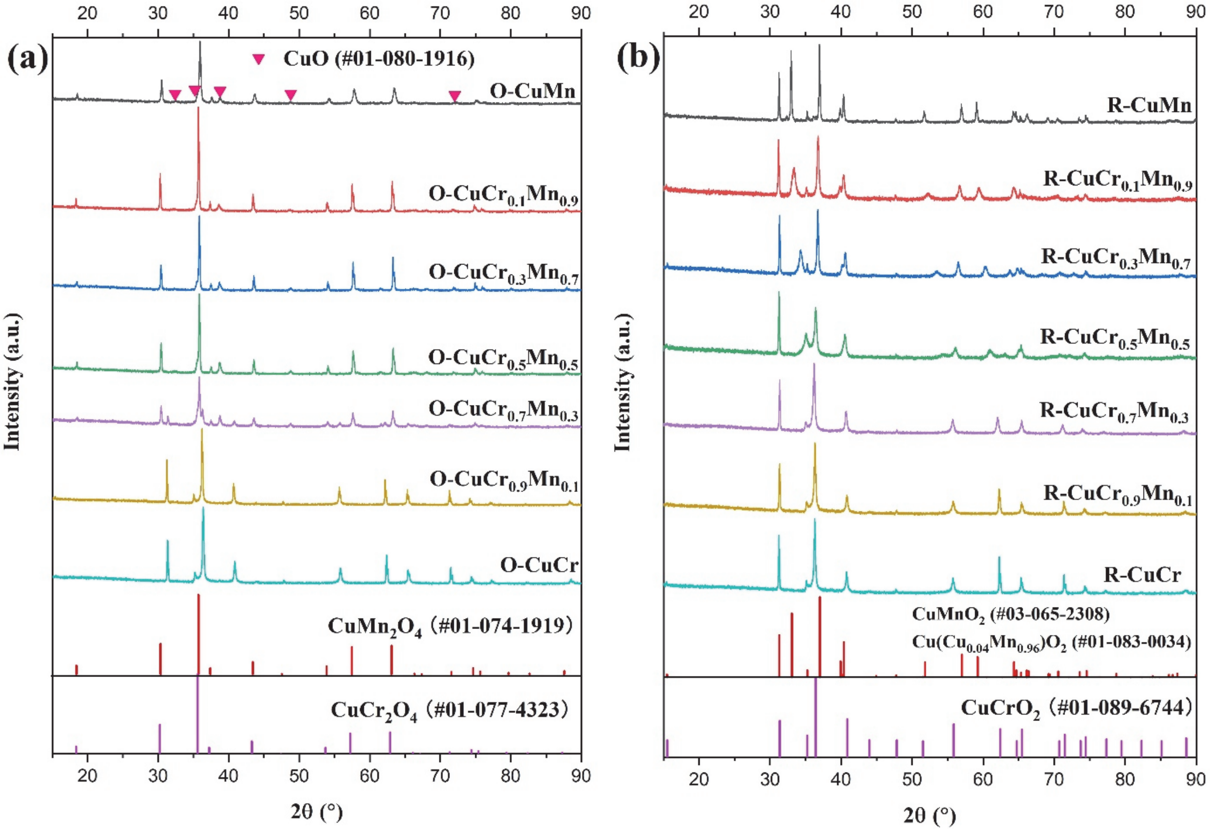

Figure 2 XRD patterns of each sample, (a): O-$CuCr_xMn_{1-x}$; (b): R-$CuCr_xMn_{1-x}$

R-CuMn exhibited two similar phases $CuMnO_2$ (03-065-2308) and $Cu(Cu_{0.04}Mn_{0.96})O_2$ (01-083-0034), which corresponds to our previous studies on Cu-based spinel material[15]. Huang et al.[24] found that during the heating process of spinel-type $CuMn_2O_4$, the material will easily turn to $Cu_{1+y}Mn_{1-y}O_2$. However, the influence of secondary phases can be ignored in this study. In contrast to spinel-type $CuMn_2O_4$ and $CuCr_2O_4$, the delafossite-type $CuMnO_2$ and $CuCrO_2$ possess their unique characteristic peaks. For example, the $CuCrO_2$ exhibited special peaks (2θ = 55.7°, 62.3°, 65.3°, 71.4°, and 74.3°) that were absent in $CuMnO_2$. It should be noted that some characteristic peaks of $CuMnO_2$ shifted and broadened as the Cr content increased, implying that its crystal structure also changed.

The magnified XRD patterns of R-CuMn, R-$CuCr_{0.1}Mn_{0.9}$, and R-$CuCr_{0.3}Mn_{0.7}$ (Figure 3a) show that the peaks at 31° (002), 33° (200), and 37° ($\bar{1}11$) shifted in different directions and exhibited an intensity that high enough for crystal lattice constants calculation. The actual lattice constants of the three materials were calculated using the standard PDF card of $CuMnO_2$ (#03-065-2308) and the results are shown in Figure 3b. The lattice constants (*a*, *b*, and *c*) of the sample deviated sightly from standard values. With the increase in Cr addition, *a* and *b* exhibited a decreasing and increasing trends, respectively. Interestingly, *c* showed a rising trend followed by a decreasing trend, which leads to R-$CuCr_{0.1}Mn_{0.9}$ possessing the largest unit cell volume among three samples (91.53 Å^3 for standard

$CuMnO_2$; 92.97 Å^3 for R-CuMn; 93.30 Å^3 for R-$CuCr_{0.1}Mn_{0.9}$; 91.48 Å^3 for R-$CuCr_{0.3}Mn_{0.7}$). Such variations may cause differences in redox behavior, heat storage capacity, etc.

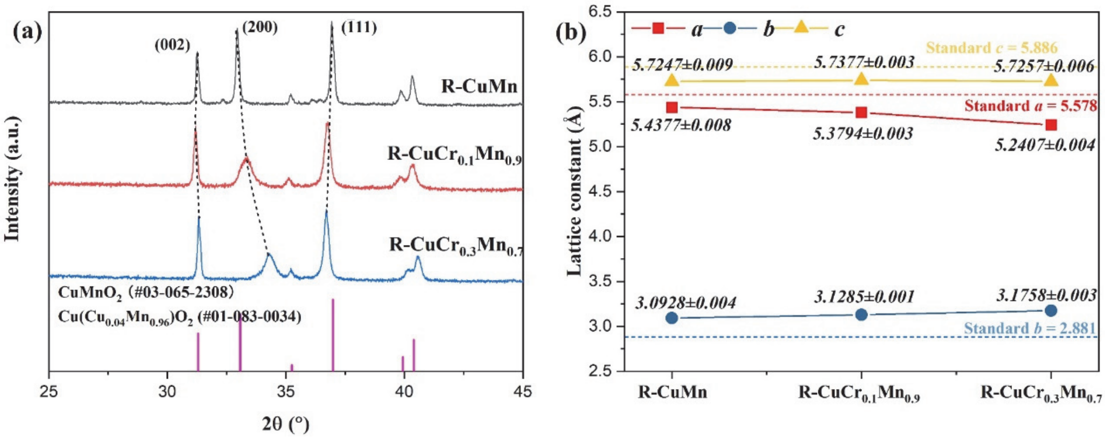

Figure 3 (a) Magnified XRD pattern of R-$CuCr_xMn_{1-x}$ (x = 0, 0.1, 0.3); (b) Lattice constants (*a*, *b*, and *c*) of R-$CuCr_xMn_{1-x}$ (x = 0, 0.1, 0.3) and standard values of $CuMnO_2$

3.2 Redox behavior

The redox behavior of each sample is shown in Figure 4. As shown in Figure 4a, when the amount of added Cr ranged from 0 to 0.5, a larger mass change was observed in the redox experiment as the amount of Cr increased. However, O-$CuCr_{0.9}Mn_{0.1}$ and O-CuCr did not show any redox capacity during the heating and cooling processes, which corresponds to the XRD results indicating that they are already in a reduced state. O-$CuCr_{0.7}Mn_{0.3}$ exhibited re-oxidation behavior in the temperature range of 550 – 750 °C because its reduction state was also existing. However, after O-$CuCr_{0.7}Mn_{0.3}$ was completely reduced into its reduction state, it is difficult to oxidize again in a short time.

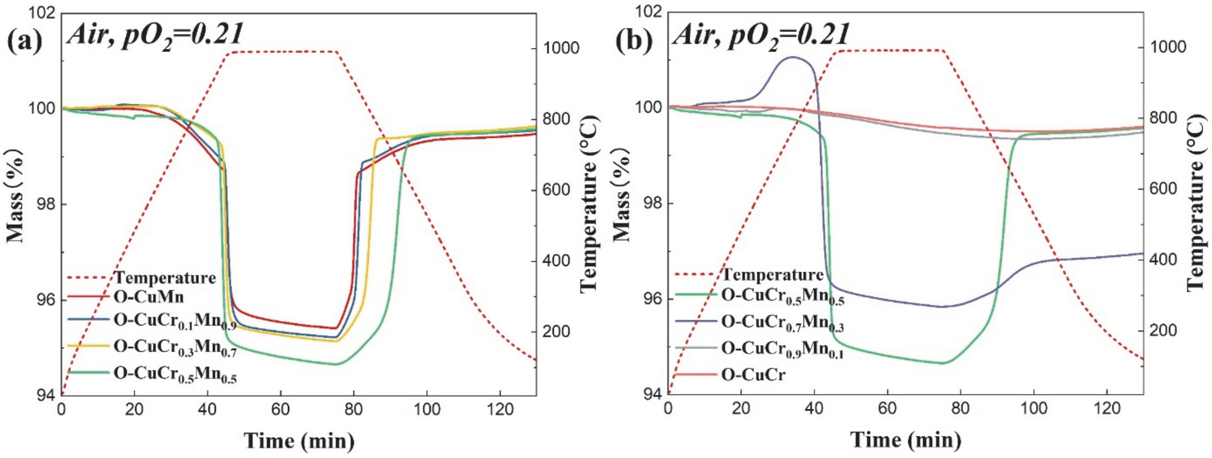

Figure 4 Redox behaviors of O-$CuCr_xMn_{1-x}$, (a): x = 0 – 0.5; (a): x = 0.5 – 1

On the other hand, we noticed that when at temperatures lower than approximately 900 °C, each material exhibited various oxygen non-stoichiometric behaviors (the mass showed a quasi-linear change with increasing temperature), which also occur in other spinel-type materials[25,26]. However, they be attributed to the phase transition between $Cu(Cr_xMn_{1-x})_2O_4$ and $CuCr_xMn_{1-x}O_2$. The change in mass exhibited by the non-stoichiometry decreased as the amount of Cr increased.

The mass change, reduction starting temperature, and oxidation ending temperature of each redoxable sample are summarized in Table 2. Importantly, the reduction starting temperatures of the Cr-doped material were slightly lower than those of pure $CuMn_2O_4$, which corresponds to the Cu-Cr-O (Fig. S1)[27] and Cu-Mn-O (Fig. S2)[15,28] phase diagrams that $CuMn_2O_4$ requires higher temperature (920 °C) for reduction than $CuCr_2O_4$ (782 °C). However, the oxidation ending temperature exhibited a larger variation as the amount of Cr increased, which led to a larger temperature hysteresis.

Table 2 Summary of the properties of redoxable samples

Sample	**Mass Change (%)**	**Reduction Starting Temp. (°C)**	**Oxidation Ending Temp. (°C)**
O-CuMn	4.57	969	883
O-$CuCr_{0.1}Mn_{0.9}$	4.78	966	859
O-$CuCr_{0.3}Mn_{0.7}$	4.86	956	784
O-$CuCr_{0.5}Mn_{0.5}$	5.34	934	611

We discussed the redox mechanism of Cu-Mn spinel oxides in our previous study[15], in which the oxidized state spinel was completely converted to reduced state delafossite ($Cu_{1+y'}Mn_{1-y'}O_2$) and a small amount of another type of spinel ($Cu_{x'}Mn_{3-x'}O_4$) during heating ([Eq.3]). In the reduction reaction of spinel, the oxygen atoms in the lattice are released in the form of oxygen. Therefore, the mass change reflected in the TGA curves can be considered as the amount of released oxygen.

$$CuMn_2O_4 + CuO \Leftrightarrow 2aCu_{x'}Mn_{3-x'}O_4 + (2-a)Cu_{1+y'}Mn_{1-y'}O_2 + (\frac{2-a}{2})O_2 \qquad (3)$$

where $\alpha = 2y'/(3 + 3y' - 2x')$.

In the O-$CuCr_xMn_{1-x}$ system considered in this study, the Cr element substituted part of the Mn element and the ratio of Cu : (Cr + Mn) was set to 1:1. To avoid introducing too many unknown parameters, the reaction equation of our sample can be simplified into [Eq.4] (Spinel for O-$CuCr_xMn_{1-x}$; Spinel’ for another type of spinel; Delafossite for R-$CuCr_xMn_{1-x}$). Spinel’ can be considered as the product of the non-stoichiometric reactions mentioned above. If the reaction does not produce another type of spinel, then the [Eq.4] can be rewritten as [Eq.5].

It is interesting to note that the stoichiometric coefficient of oxygen is determined by the value of a; in other words, the amount of oxygen released is determined by the product ratio of another type of spinel and delafossite.

$$\boldsymbol{Spinel} + CuO \Leftrightarrow\ 2a\,\boldsymbol{Spienl'} + (2-a)\boldsymbol{Delafossite} + \frac{1-2a}{2}O_2 \tag{4}$$

$$\boldsymbol{Spinel} + CuO \Leftrightarrow\ 2\boldsymbol{Delafossite} + \frac{1}{2}O_2 \tag{5}$$

As the amount of added Cr increased, the redoxable sample exhibited a larger change in mass (Figure 3, Table 2), indicating that more oxygen was released, namely a smaller value of a was attained. From [Eq.4], it is clear that the production of another type of spinel is reduced and more delafossite is formed when Cr is added. From the perspective of phase change, the transition between spinel and delafossite may involve a larger energy conversion than that between different types of spinels; hence, fewer non-stoichiometric reactions are preferable. In conclusion, Cr plays an important role in controlling the formation of spinel and delafossite, which may also affect the heat storage capacity of the material.

3.3 Re-oxidation behavior and kinetics calculation

The re-oxidation behavior of R-$CuCr_xMn_{1-x}$ is shown in Figure 5. R-$CuCr_{0.9}Mn_{0.1}$ and R-CuCr do not show any re-oxidation capacity during the non-isothermal heating process in a ramp of 20 °C/min. The lack of reversibility may be directly related to the oxygen partial pressure, where the ΔG for the re-oxidation of R-$CuCr_{0.9}Mn_{0.1}$ and R-CuCr under air (pO_2 = 0.21) is always greater than 0 thus preventing a spontaneous reaction.

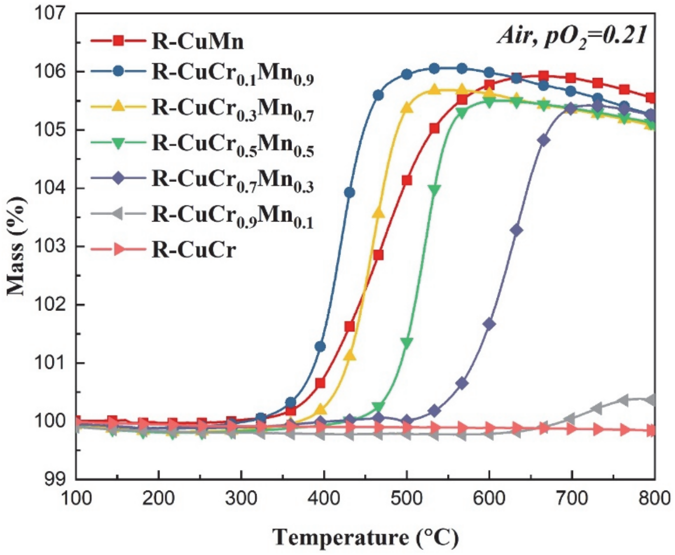

Figure 5 Re-oxidation behaviors of R-$CuCr_xMn_{1-x}$

The most interesting aspect of Figure 5 is that the Cr-doped sample (x ≤ 0.7) exhibits a faster reaction rate than R-CuMn because the slope of each curve can be regarded as the reaction rate when heating ramp is fixed. Furthermore, the re-oxidation reaction of R-$CuCr_{0.1}Mn_{0.9}$ occurred at a lower temperature (305 °C) than that of R-CuMn (337 °C). However, R-$CuCr_{0.5}Mn_{0.5}$ and R-$CuCr_{0.7}Mn_{0.3}$ require higher temperatures for their re-oxidation reactions although their reaction rates exceeded than those of R-CuMn.

For further investigation, a re-oxidation kinetic analysis was performed. Gas-solid reactions can be described by an Arrhenius-type law ([Eq.6]).

$$r = \frac{d\alpha}{dt} = Aexp\left(\frac{-E_a}{RT}\right) f(\alpha) \tag{6}$$

where α is the conversion ratio, A is the pre-exponential factor, E_a is the activation energy, R is the gas constant, and $f(\alpha)$ is the reaction model.

The re-oxidation activation energy (E_a) of R-$CuCr_xMn_{1-x}$ (x = 0, 0.1, 0.3) was calculated using a non-isothermal method. Based on TGA data of a reaction occurring with mass loss, the conversion ratio α is obtained from [Eq.7]:

$$\alpha = \frac{m_0 - m_t}{m_0 - m_f} \tag{7}$$

where m_0 is initial mass, m_t is weight at certain time t, and m_f is final mass.

Figure 6a, b depicts the α-time *and* α-Temperature plots of a typical re-oxidation reaction of R-CuMn. From these plots, it is possible to determine re-oxidation E_a using the Friedman method[29] ([Eq.8]) which is recommended by ICTAC[30].

$$\ln\left(\beta\frac{\mathrm{d}\alpha}{\mathrm{d}T}\right) = \ln[Af(\alpha)] - \frac{E_a}{RT} \tag{8}$$

where β is the heating ramp, A is the pre-exponential factor, $f(\alpha)$ is the reaction model, E_a is the activation energy, and R is the gas constant.

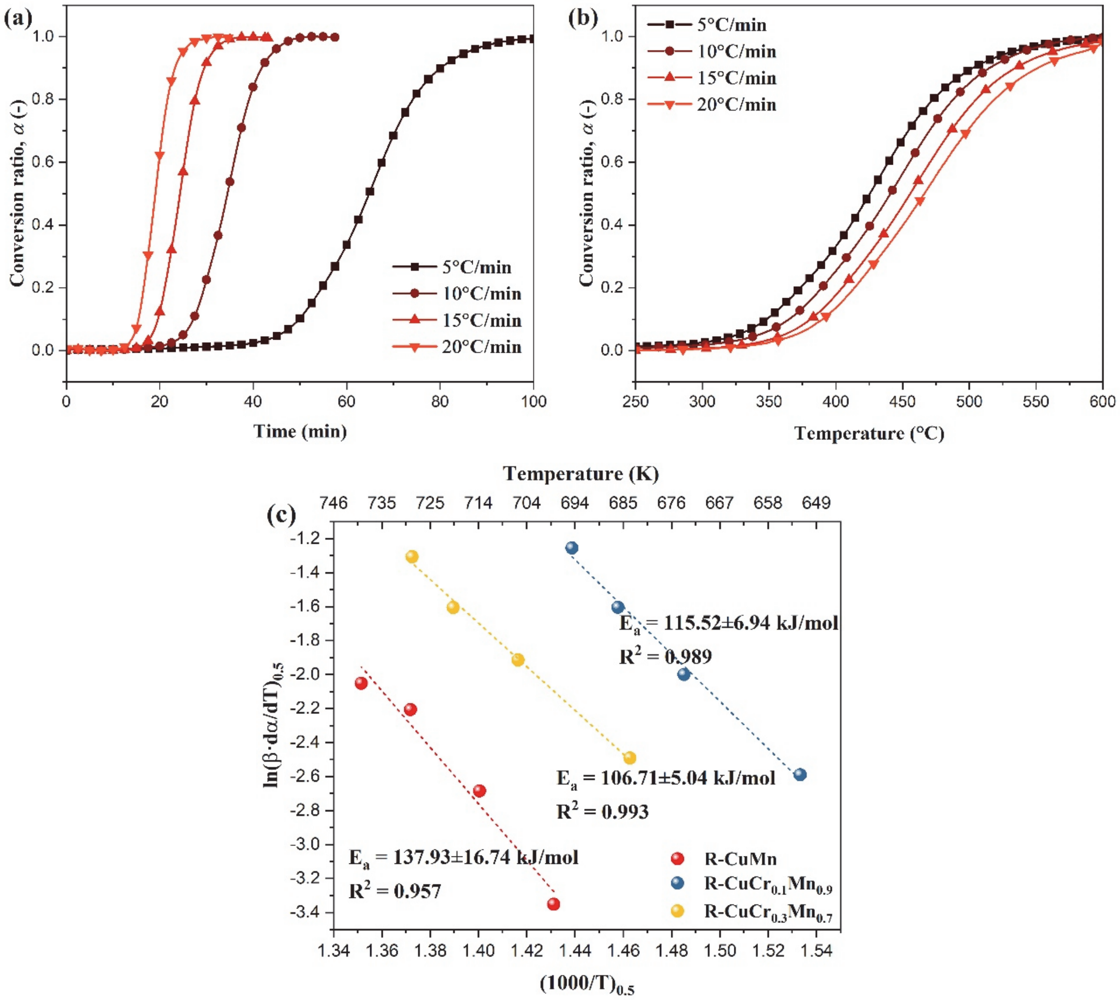

Figure 6 (a) Typical α-time plots for R-CuMn; (b) Typical α-temperature plots for R-CuMn; (c) Arrhenius plot of E_a for R-CuCr$_x$Mn$_{1\text{-}x}$ (x = 0, 0.1, 0.3)

The Friedman method allows the estimation of E_a without prior knowledge of $f(\alpha)$ because the plot of the left term of [Eq.8] versus 1/T yields E_a from the slope of the fitted curve. An Arrhenius plot of E_a for each sample at $\alpha = 0.5$ is shown in Figure 6c. R-CuCr$_{0.1}$Mn$_{0.9}$ and R-CuCr$_{0.3}$Mn$_{0.7}$ exhibited smaller re-oxidation E_a (115.52 ± 6.94 kJ/mol and 106.71 ± 5.04 kJ/mol, respectively) than R-CuMn (137.93 ± 16.74 kJ/mol). These results imply that Cr element may reduce the activation energy of the re-oxidation reaction and accelerate the reaction, which also corresponds to the behavior shown in Figure 5.

Once the activation energy E_a was determined, the model and mechanism of the reaction can be investigated by using the g(α)/g(0.5) master plots. Eq.9 holds under non-isothermal conditions (more details are provided in the supplementary document). Introducing the average value of E_a which is computed using the Friedman method, the experimental data extracted from the TGA results (the left term of Eq.9) may be plotted in the theoretical g(α)/g(0.5) master plots (right term of Eq.9).

$$\frac{\theta}{\theta_{0.5}} = \frac{g(\alpha)}{g(\alpha)_{0.5}} \tag{9}$$

where θ is the generalized time and g(α) is the integral form of kinetic rate equation. The subscript of 0.5 indicates that these terms assume value when α is 0.5. By Comparing the experimental data with theoretical master plot, the best-fitting model was adopted.

The master plots of R-CuMn, R-$CuCr_{0.1}Mn_{0.9}$, and R-$CuCr_{0.3}Mn_{0.7}$ with different heating ramps are depicted in Fig.S3, Fig.S4, and Fig.S5, respectively. The α-time *and* α-Temperature plots in Figure 6a and Figure 6b show that the material exhibited a sigmoid curve that could be ascribed to nucleation and growth mechanisms during re-oxidation. The master plot results also supported this hypothesis, although the curves of R-$CuCr_{0.1}Mn_{0.9}$ and R-$CuCr_{0.3}Mn_{0.7}$ deviated sightly from pure thermotical model depending on the conversion ratio. After careful consideration, the three-dimensional diffusion (D3), contracting sphere (R3), and contracting cylinder (R2) models were assigned to R-CuMn, R-$CuCr_{0.1}Mn_{0.9}$, and R-$CuCr_{0.3}Mn_{0.7}$, respectively.

The pre-exponential factor A can be generated from E_a and $f(\alpha)$ using the intercept of Eq.8. Owing to different heating ramps, A may vary within a certain range, even for the same sample. Therefore, the average value of A was used for a general description. The kinetic triplet parameters (A, E_a, and f(α)) of R-$CuCr_xMn_{1-x}$ (x = 0, 0.1, and 0.3) are summarized in Table 3.

Table 3 Kinetic parameters of R-$CuCr_xMn_{1-x}$ (x = 0, 0.1, 0.3)

Sample	A (min^{-1})	E_a ($kJ \cdot mol^{-1}$)	Reaction model	$f(\alpha)$
R-CuMn	1.70×10^8	137.93	D3	$\frac{3(1-\alpha)^{2/3}}{2(1-(1-\alpha)^{1/3})}$
R-$CuCr_{0.1}Mn_{0.9}$	6.90×10^7	115.52	R3	$3(1-\alpha)^{2/3}$
R-$CuCr_{0.3}Mn_{0.7}$	8.26×10^6	106.71	R2	$2(1-\alpha)^{1/2}$

As mentioned above, Cr doping contributed to the decrease in re-oxidation activation energy. On the other hand, the reaction model of the sample was also changed from the oxygen diffusion-controlled to contracting-controlled mechanism because of the introduction of Cr.

A detailed description of different reaction models can be found in the work of Khawam et al[31]. In diffusion (D) models, solid-state reactions often occur between crystal lattices or molecules that have to permeate into the lattice. Therefore, the motion of atoms is restricted because it depends on lattice defects. However, geometrical contraction (R) models assume that nucleation occurs rapidly on the surface of the crystal, and that the rate of contraction is controlled by the progress of resulting reaction interface toward the center of the crystal. It should be noted that the D3 (R-CuMn) and R3 (R-

$CuCr_{0.1}Mn_{0.9}$) models are based on the assumption of spherical solid particles, whereas the R2 model (R-$CuCr_{0.3}Mn_{0.7}$) is based on the assumption of cylinder particles. The SEM morphology of R-CuMn, R-$CuCr_{0.1}Mn_{0.9}$, and R-$CuCr_{0.3}Mn_{0.7}$ (Fig.S6) confirm that the material changes from massive particles to fine strip particles with increasing amount of added Cr, which is also consistent with the assumptions of the models. In addition, examples of changes in the material reaction model owing to the addition of other elements can also be found in Fe-doped Mn_2O_3/Mn_3O_4 which was investigated by Carrillo et al[32].

The accuracy of our kinetic model was verified by performing a series of predictions based on the model (Figure 7). The kinetic model of R-CuMn exhibited a good agreement with the experimental data; however, the predictions of R-$CuCr_{0.1}Mn_{0.9}$ and R-$CuCr_{0.3}Mn_{0.7}$ slightly deviated from the experiment because their curves did not fit well with the pure theoretical reaction model in the master plots. This also implies that the selection of reaction model in the previous step profoundly affects on the accuracy of kinetic predictions.

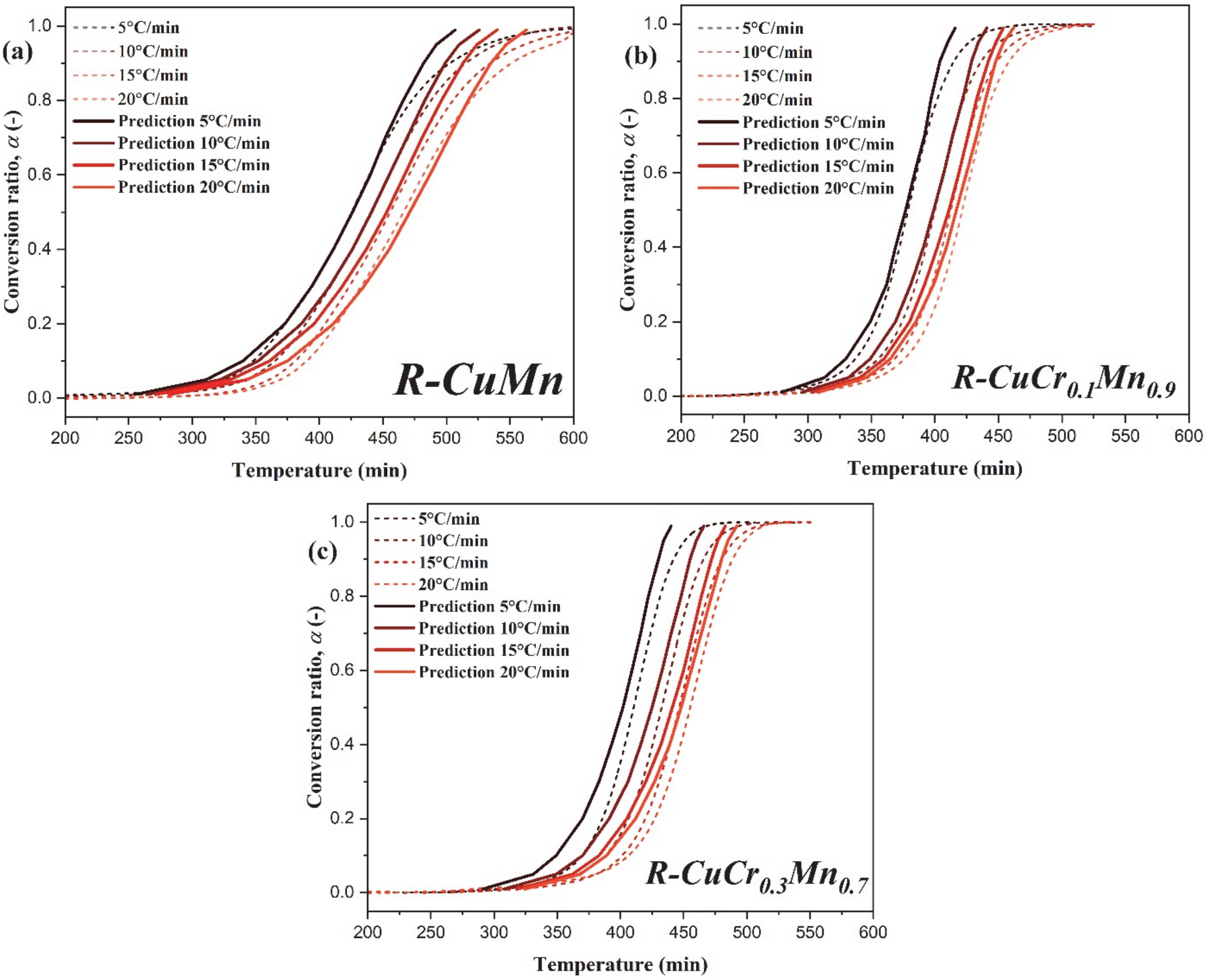

Figure 7 (a) Kinetic prediction of R-CuMn; (b) Kinetic prediction of R-$CuCr_{0.1}Mn_{0.9}$; (c) Kinetic prediction of R-$CuCr_{0.1}Mn_{0.9}$

However, the mechanism that why the Cr-added sample can re-oxidize more easier than R-CuMn remains unclear. The crystal structures of $CuMnO_2$ and $CuCrO_2$ are shown in Figure 8. The crednerite $CuMnO_2$ exhibits a monoclinic structure at room temperature, consisting of edge-shared MO_6 octahedra and two-coordinated Cu^+ cations at the interlayer sites. The $CuCrO_2$ exhibits a trigonal structure, which also consists of edge-shared MO_6 octahedra and only one Cu^+ cation at the interlayer sites. The addition of Cr may reduce the amount of Cu^+ cation at the interlayer sites in some crystal lattices. From the perspective of space-filling, it provides more empty space for the intake/release of oxygen from crystal lattice which accelerates the re-oxidation rate.

On the other hand, as calculated from the magnified XRD patterns of R-$CuCr_xMn_{1-x}$ (x = 0, 0.1, 0.3), R-$CuCr_{0.1}Mn_{0.9}$ (Figure 3) exhibited the largest unit cell volume (93.30 Å^3) among three samples. We infer that R-$CuCr_{0.1}Mn_{0.9}$ exhibited better kinetic performance in macro scale and lower re-oxidation starting temperature among all sample because of the combined effect of a larger unit cell volume and more free space.

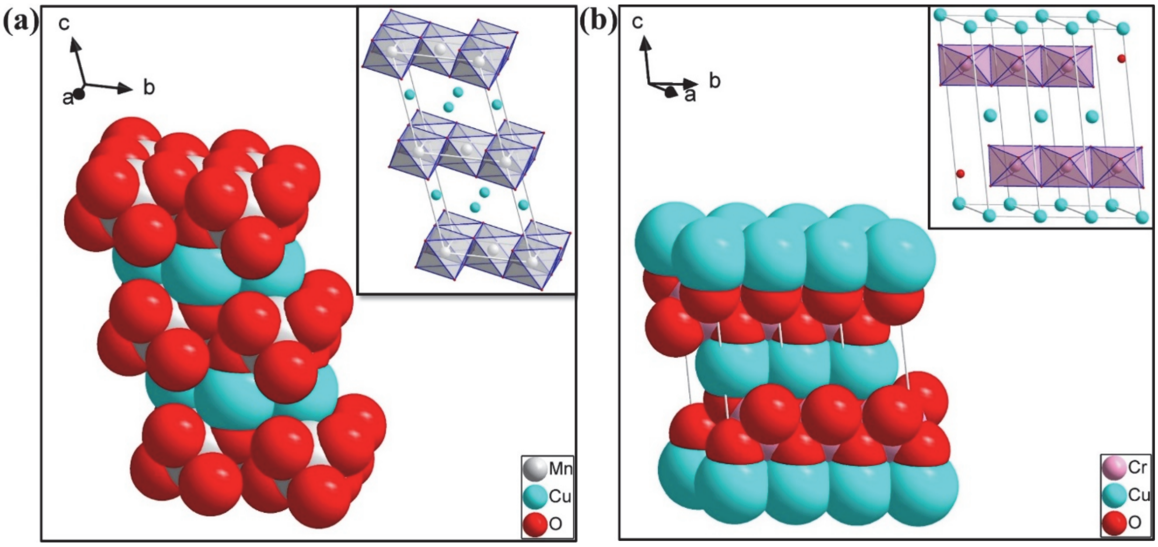

Figure 8 Schematic of the crystal structure of (a): $CuMnO_2$; (b): $CuCrO_2$

3.4 Oxidation enthalpy

The redoxable sample R-$CuCr_xMn_{1-x}$ (x = 0, 0.1, 0.3, 0.5) was chosen for oxidation enthalpy measurements using isothermal oxidation method. A typical DSC curve of R-CuMn is shown in Figure 9a, where a sharp exothermic peak associated with the oxidation reaction can be observed in the DSC curve. According to Figure 9b, the oxidation enthalpies of each sample are: 236.11 ± 5.40 kJ/kg (1.30 ± 0.03 MJ/L) for R-CuMn, 293.67 ± 1.25 kJ/kg (1.62 ± 0.01 MJ/L) for R-$CuCr_{0.1}Mn_{0.9}$, 305.61 ± 16.45 kJ/kg (1.68 ± 0.09 MJ/L) for R-$CuCr_{0.3}Mn_{0.7}$, and 292.59 ± 7.00 kJ/kg (1.61 ± 0.04 MJ/L) for R-$CuCr_{0.5}Mn_{0.5}$. As the amount of Cr increases, the heat storage capacity of the material initially increases and then decreases. This implies that a small amount of Cr improves the heat storage capacity of the material. However, when the amount of Cr exceeds a certain value (x > 0.3), the non-redox property embodied by $CuCrO_2$ dominates. This reduces the heat storage capacity or even hinders the re-oxidation behavior of the material.

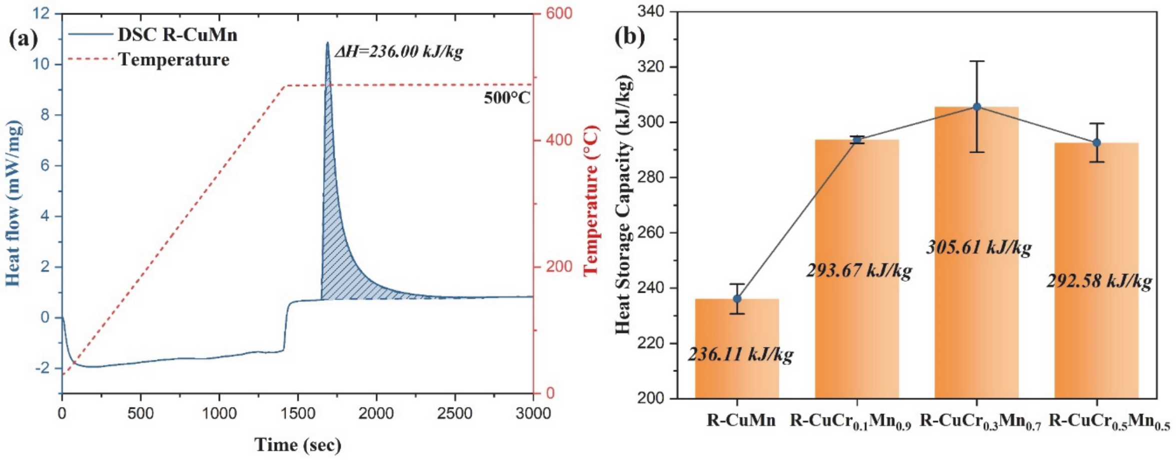

Figure 9 (a) Typical DSC curve of R-CuMn (re-oxidation in air, pO_2 =0.21); (b) Oxidation enthalpies of R-$CuCr_xMn_{1-x}$ (x = 0, 0.1, 0.3, 0.5)

3.5 Cyclability test

O-$CuCr_{0.1}Mn_{0.9}$ and O-$CuCr_{0.3}Mn_{0.7}$ were chosen for 20 cycles cyclability test in the range of 500 – 1000 °C owing to the favorable redox behavior and larger heat storage capacity. To investigate the effect of Cr addition on the cyclability of the material, a cyclability test of O-CuMn was also performed using the same TGA heating/cooling program. Figure 10a shows a typical TGA program of O-CuMn.

The mass change (Δm) of each sample (for temperature ranging from 500 – 1000 °C) is summarized in Figure 10b. Although O-CuMn and O-$CuCr_{0.1}Mn_{0.9}$ exhibited stable changes in mass over the 20 cycles test, O-$CuCr_{0.3}Mn_{0.7}$ showed more fluctuating behavior. In our previous work, O-CuMn exhibited a "run-in" period where its mass change was unstable before 13 cycles[15]. This can be attributed to the different synthesis conditions of heating temperature (960 °C and 1000 °C for the previous and present study, respectively). The XRD patterns of each sample before and after 20 cycles (Figure 10c) shows that the samples did not produce side phases in the cyclability experiment, which indicated their good compositional stability. In conclusion, a small amount of Cr ($x \leq 0.3$) did not negatively affect the cyclability of the material but resulted in faster kinetics, lower operating temperature, and larger heat storage capacity.

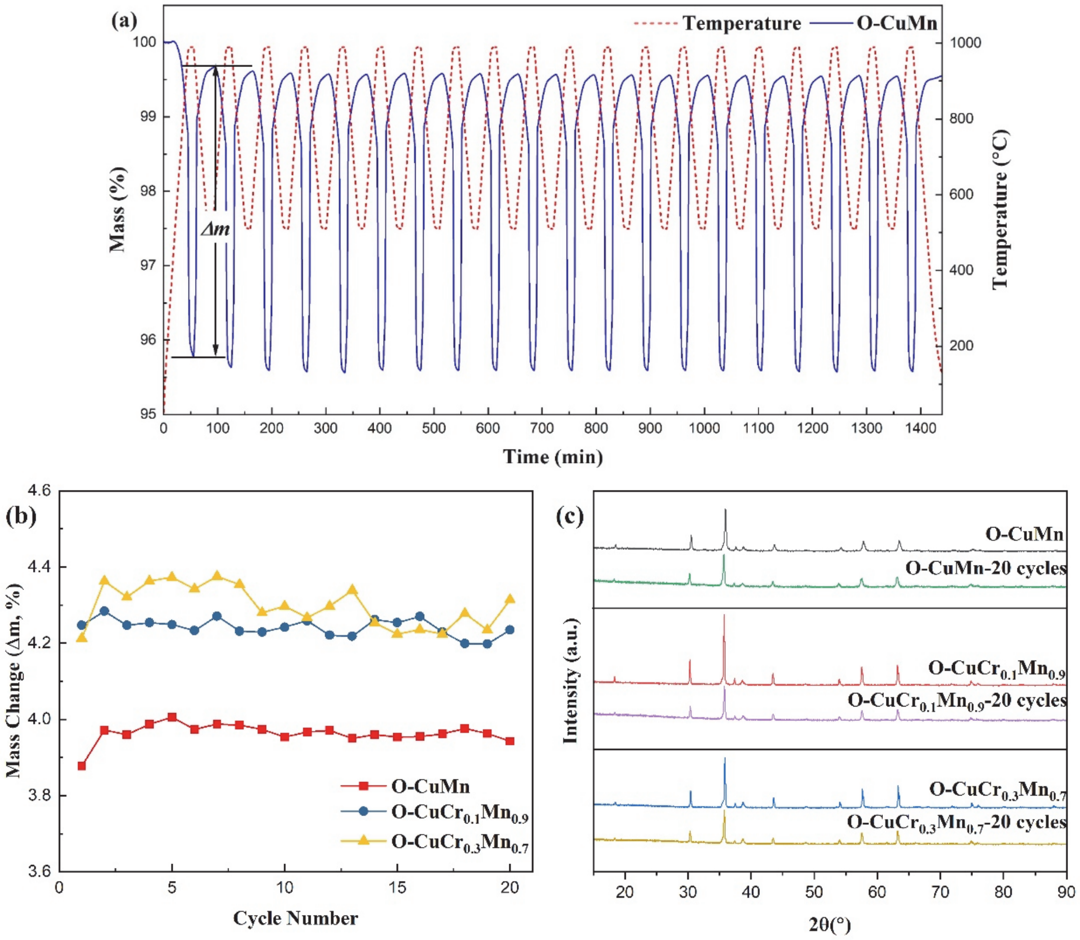

Figure 10 (a) Typical 20 cycles TGA program of O-CuMn in synthetic air (500-1000 °C), for a holding time of 10 mins; (b) Summary of mass changes of each sample during the 20 cycles test; (c) Comparison of the XRD pattern of each sample before and after cycling

4. Conclusions

In redox-type TCES systems, the reaction medium (oxygen) can be extracted from the atmosphere, which provides economic and volume advantages to its applications. However, the inherent high operating temperatures of metal oxides limits the application of redox-type TCES is limited to high temperatures (> 1000 °C) for CSP purposes. In this study, we implemented the concept of a medium-high temperature (500 – 1000 °C) TCES system and developed $Cu(Cr_xMn_{1-x})_2O_4/CuCr_xMn_{1-x}O_2$ for this purpose. The Pechini method was applied to synthesize all samples because of its precise component controllability. The structural characteristics of all samples were investigated using XRD. Except for O-$CuCr_{0.7}Mn_{0.3}$ and O-$CuCr_{0.9}Mn_{0.1}$, most of samples were successfully prepared through Pechini method because the Cr-rich samples lacked redox ability. In redox experiments, Cr-added samples exhibited reduced operating temperature and controllable oxygen non-stoichiometric properties. R-$CuCr_{0.1}Mn_{0.9}$ and R-$CuCr_{0.3}Mn_{0.7}$ showed faster reaction rates than R-CuMn because Cr-doped sample required lower activation energy (E_a) for re-oxidation (115.52 ± 6.94 kJ/mol and 106.71 ± 5.04 kJ/mol for R-$CuCr_{0.1}Mn_{0.9}$ and R-$CuCr_{0.3}Mn_{0.7}$; 137.93 ± 16.74 kJ/mol for R-CuMn). Furthermore, the reaction model changed from D3 to R3 and then to R2 as the amount of Cr doping increased. Later, we proposed the combined effect of larger unit cell volume and more free space as a possible reason for the re-oxidation of R-$CuCr_{0.1}Mn_{0.9}$ at lower temperatures.

Although the reduction and oxidation temperatures were reduced by Cr doping, they were still insufficient compared to our expected values. But to our surprise, the results of DSC enthalpy measurement indicated an appropriate amount of Cr helps in improving the heat storage capacity of the material. In the cyclability test, the addition of a small amount of Cr did not cause the deterioration of cyclic properties. A comparison of XRD patterns of each sample before and after cycling was performed to verify this result. In particular, O-CuMn and O-$CuCr_{0.1}Mn_{0.9}$ exhibited stable changes in mass over the 20 cycles test; however, O-$CuCr_{0.3}Mn_{0.7}$ showed more fluctuation.

In conclusion, we demonstrated that the addition of other elements affected the reaction temperature, reaction kinetics, and heat storage capacity of the TCES material. This perspective provides a feasible path for the future development of new materials in the medium-high temperature TCES field.

Supporting Information

Phase diagrams; kinetic models; master plots; SEM images of R-$CuCr_xMn_{1-x}$ (x = 0, 0.1, 0.3)

Acknowledgement

This research was supported by “Knowledge Hub Aichi”, Priority Research Project (3rd term) from Aichi Prefectural Government, Japan

In addition, we would like to thank Editage (www.editage.com) for English language editing.

Reference

(1) Carrillo, A. J.; González-Aguilar, J.; Romero, M.; Coronado, J. M. Solar Energy on Demand: A Review on High Temperature Thermochemical Heat Storage Systems and Materials. *Chem. Rev.* **2019**, *119* (7), 4777–4816.

(2) Wu, S.; Zhou, C.; Doroodchi, E.; Nellore, R.; Moghtaderi, B. A Review on High-Temperature Thermochemical Energy Storage Based on Metal Oxides Redox Cycle. *Energy Convers. Manag.* **2018**, *168* (April), 421–453.

(3) Dizaji, H. B.; Hosseini, H. A Review of Material Screening in Pure and Mixed-Metal Oxide Thermochemical Energy Storage (TCES) Systems for Concentrated Solar Power (CSP) Applications. *Renew. Sustain. Energy Rev.* **2018**, *98* (May), 9–26.

(4) André, L.; Abanades, S.; Flamant, G. Screening of Thermochemical Systems Based on Solid-Gas

Reversible Reactions for High Temperature Solar Thermal Energy Storage. *Renew. Sustain. Energy Rev.* **2016**, *64*, 703–715.

(5) Imponenti, L.; Albrecht, K. J.; Wands, J. W.; Sanders, M. D.; Jackson, G. S. Thermochemical Energy Storage in Strontium-Doped Calcium Manganites for Concentrating Solar Power Applications. *Sol. Energy* **2017**, *151*, 1–13.

(6) Agrafiotis, C.; Roeb, M.; Schmücker, M.; Sattler, C. Exploitation of Thermochemical Cycles Based on Solid Oxide Redox Systems for Thermochemical Storage of Solar Heat. Part 1: Testing of Cobalt Oxide-Based Powders. *Sol. Energy* **2014**, *102*, 189–211.

(7) Wokon, M.; Kohzer, A.; Linder, M. Investigations on Thermochemical Energy Storage Based on Technical Grade Manganese-Iron Oxide in a Lab-Scale Packed Bed Reactor. *Sol. Energy* **2017**, *153*, 200–214.

(8) Mastronardo, E.; Qian, X.; Coronado, J. M.; Haile, S. M. The Favourable Thermodynamic Properties of Fe-Doped CaMnO3for Thermochemical Heat Storage. *J. Mater. Chem. A* **2020**, *8* (17), 8503–8517.

(9) Tescari, S.; Singh, A.; Agrafiotis, C.; de Oliveira, L.; Breuer, S.; Schlögl-Knothe, B.; Roeb, M.; Sattler, C. Experimental Evaluation of a Pilot-Scale Thermochemical Storage System for a Concentrated Solar Power Plant. *Appl. Energy* **2017**, *189*, 66–75.

(10) Yilmaz, D.; Darwish, E.; Leion, H. Utilization of Promising Calcium Manganite Oxygen Carriers for Potential Thermochemical Energy Storage Application. *Ind. Eng. Chem. Res.* **2021**, *60* (3), 1250–1258.

(11) Schrader, A. J.; Schieber, G. L.; Ambrosini, A.; Loutzenhiser, P. G. Experimental Demonstration of a 5 KWth Granular-Flow Reactor for Solar Thermochemical Energy Storage with Aluminum-Doped Calcium Manganite Particles. *Appl. Therm. Eng.* **2020**, *173* (March), 115257.

(12) Chen, X.; Kubota, M.; Yamashita, S.; Kita, H. Investigation of Sr-Based Perovskites for Redox-Type Thermochemical Energy Storage Media at Medium-High Temperature. *J. Energy Storage* **2021**, *38* (November 2020), 102501.

(13) Kato, S.; Fujimaki, R.; Ogasawara, M.; Wakabayashi, T.; Nakahara, Y.; Nakata, S. Oxygen Storage Capacity of CuMO2 (M = Al, Fe, Mn, Ga) with a Delafossite-Type Structure. *Appl. Catal. B Environ.* **2009**, *89* (1–2), 183–188.

(14) Kato, S.; Sato, H.; Ogasawara, M.; Wakabayashi, T.; Nakahara, Y.; Nakata, S. Oxygen Storage Capacity of Delafossite-Type CuLnO 2 (Ln = La, Y) and Their Stability under Oxidative/Reductive Atomosphere. *Solid State Sci.* **2012**, *14* (1), 177–181.

(15) Chen, X.; Kubota, M.; Yamashita, S.; Kita, H. Exploring Cu-Based Spinel/Delafossite Couples for Thermochemical Energy Storage at Medium-High Temperature. *ACS Appl. Energy Mater.* **2021**, *4* (7), 7242–7249.

(16) Fan, J.; Zhang, Y.; Yang, Y.; Hao, J.; Wang, Y.; Qian, A. Performance of Thermochemical

Energy Storage for Spinel CuMn 2 O 4 Material. *J. Energy Storage* **2021**, *41* (January), 102881.

(17) Portilla-Nieto, Y.; Zaki, A.; Vidal, K.; Hernaiz, M.; Aranzabe, E.; Doppiu, S.; Faik, A. Development of Co3-XNixO4 Materials for Thermochemical Energy Storage at Lower Red-Ox Temperature. *Sol. Energy Mater. Sol. Cells* **2021**, *230* (November 2020), 111194.

(18) Eric, H.; Timuçin, M. Equilibrium Relations in the System Nickel Oxide-Copper Oxide. *Metall. Trans. B* **1979**, *10* (4), 561–563.

(19) Carrillo, A. J.; Pizarro, P.; Coronado, J. M. Assessing Cr Incorporation in Mn2O3/Mn3O4 Redox Materials for Thermochemical Heat Storage Applications. *J. Energy Storage* **2021**, *33* (July 2020), 102028.

(20) Pechini, M. P. Method of Pre Parng Lead and Alkalne Earth Titanates and Nobates and Coat. *US Pat. 3,330,697* **1967**, 2.

(21) Dey, S.; Naidu, B. S.; Rao, C. N. R. Beneficial Effects of Substituting Trivalent Ions in the B-Site of La0.5Sr0.5Mn1-XAxO3 (A = Al, Ga, Sc) on the Thermochemical Generation of CO and H2 from CO2 and H2O. *Dalt. Trans.* **2016**, *45* (6), 2430–2435.

(22) Rao, C. N. R.; Dey, S. Solar Thermochemical Splitting of Water to Generate Hydrogen. *Proc. Natl. Acad. Sci. U. S. A.* **2017**, *114* (51), 13385–13393.

(23) Song, Z.; Liu, Q. Tolerance Factor and Phase Stability of the Normal Spinel Structure. *Cryst. Growth Des.* **2020**, *20* (3), 2014–2018.

(24) Huang, X.; Ni, C.; Zhao, G.; Irvine, J. T. S. Oxygen Storage Capacity and Thermal Stability of the CuMnO2-CeO2 Composite System. *J. Mater. Chem. A* **2015**, *3* (24), 12958–12964.

(25) Lisboa-Filho, P. N.; Bahout, M.; Barahona, P.; Moure, C.; Peña, O. Oxygen Stoichiometry Effects in Spinel-Type NiMn2O 4-δ Samples. *J. Phys. Chem. Solids* **2005**, *66* (7), 1206–1212.

(26) Bulavchenko, O. A.; Venediktova, O. S.; Afonasenko, T. N.; Tsyrul'Nikov, P. G.; Saraev, A. A.; Kaichev, V. V.; Tsybulya, S. V. Nonstoichiometric Oxygen in Mn-Ga-O Spinels: Reduction Features of the Oxides and Their Catalytic Activity. *RSC Adv.* **2018**, *8* (21), 11598–11607.

(27) Schorne-Pinto, J.; Chartrand, P.; Barnabé, A.; Cassayre, L. Thermodynamic and Structural Properties of CuCrO2and CuCr2O4: Experimental Investigation and Phase Equilibria Modeling of the Cu-Cr-O System. *J. Phys. Chem. C* **2021**, *125* (27), 15069–15084.

(28) Driessens, F. C. M. Phase Equilibria in the System Cu-Mn-O. *Zeitschrift für Anorg. und Allg. Chemie* **1967**, *351* (1–2), 48–62.

(29) Friedman, H. L. Kinetics of Thermal Degradation of Char-Forming Plastics from Thermogravimetry. Application to a Phenolic Plastic. *J. Polym. Sci. Part C Polym. Symp.* **1967**, *6* (1), 183–195.

(30) Vyazovkin, S.; Burnham, A. K.; Criado, J. M.; Pérez-Maqueda, L. A.; Popescu, C.; Sbirrazzuoli, N. ICTAC Kinetics Committee Recommendations for Performing Kinetic Computations on Thermal Analysis Data. *Thermochim. Acta* **2011**, *520* (1–2), 1–19.

(31) Khawam, A.; Flanagan, D. R. Solid-State Kinetic Models: Basics and Mathematical Fundamentals. *J. Phys. Chem. B* **2006**, *110* (35), 17315–17328.

(32) Carrillo, A. J.; Serrano, D. P.; Pizarro, P.; Coronado, J. M. Understanding Redox Kinetics of Iron-Doped Manganese Oxides for High Temperature Thermochemical Energy Storage. *J. Phys. Chem. C* **2016**, *120* (49), 27800–27812.